

# Self-Assembled Nanoparticle Drumhead Resonators

Pongsakorn Kanjanaboos,<sup>†</sup> Xiao-Min Lin,<sup>§</sup> John E. Sader,<sup>||,⊥</sup> Sara M. Rupich,<sup>‡</sup> Heinrich M. Jaeger,<sup>†</sup> and Jeffrey R. Guest<sup>\*,§</sup>

<sup>†</sup>James Franck Institute and Department of Physics and <sup>‡</sup>James Franck Institute and Department of Chemistry, The University of Chicago, 929 E. 57th St., Chicago, Illinois 60637, United States

<sup>§</sup>Center for Nanoscale Materials, Argonne National Laboratory, Argonne, Illinois 60439, United States

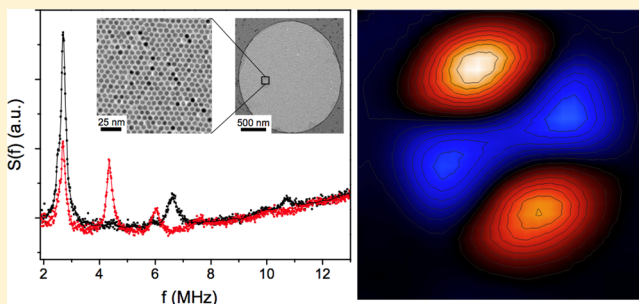
<sup>||</sup>Department of Mathematics and Statistics, The University of Melbourne, Victoria 3010, Australia

<sup>⊥</sup>Kavli Nanoscience Institute and Department of Physics, California Institute of Technology, Pasadena, California 91125, United States

## Supporting Information

**ABSTRACT:** The self-assembly of nanoscale structures from functional nanoparticles has provided a powerful path to developing devices with emergent properties from the bottom-up. Here we demonstrate that freestanding sheets self-assembled from various nanoparticles form versatile nanomechanical resonators in the megahertz frequency range. Using spatially resolved laser-interferometry to measure thermal vibrational spectra and image vibration modes, we show that their dynamic behavior is in excellent agreement with linear elastic response for prestressed drumheads of negligible bending stiffness. Fabricated in a simple one-step drying-mediated process, these resonators are highly robust and their inorganic–organic hybrid nature offers an extremely low mass, low stiffness, and the potential to couple the intrinsic functionality of the nanoparticle building blocks to nanomechanical motion.

**KEYWORDS:** Self-assembly, freestanding ultrathin monolayer, thin films, resonators, imaging, nanoparticles, resonance frequency, vibration modes, drumhead resonator, nanomechanics



Nanoparticle self-assembly is a versatile fabrication technique for devices with tailored electronic, optical, or structural properties.<sup>1–5</sup> In nanoparticle solids, the inorganic particle cores are typically surrounded by an organic shell of short molecules,<sup>5,6</sup> which stabilize the particles and prevent sintering of the cores when the particles form densely packed superlattices. Advances over the last several years have made it possible to assemble ultrathin nanoparticle layers at liquid–air interfaces for a wide range of different particle cores and capping ligands<sup>7–10</sup> and use this process to fabricate various freestanding nanoparticle membranes, including oleic acid capped CoO monolayers, DNA-capped Au monolayers, and binary superlattice monolayers.<sup>8,9,11–15</sup> In such membranes, the ligands also provide for high strength and large Young's modulus under tensile loads, while enabling very low bending stiffness and thus high flexibility.<sup>11–14</sup> For example, ~10 nm thin membranes, supported by a substrate only along their outer edge, can be draped by drying-mediated self-assembly (see Supporting Information, Figure S1) over holes several micrometers in diameter, thereby freely suspending >10<sup>5</sup> close-packed nanoparticles.<sup>13</sup> Despite the fact that the ligands are short (in some cases <2 nm), once attached to the nanoparticles on one end and confined in dense, possibly interdigitated arrangements inside the interstices among

particles, they imbue monolayers with Young's moduli  $E$  of several GPa without any cross-linking. At the same time, the process of sticking to the substrate, and in particular clinging to the vertical sidewalls of the hole, strains the monolayers, typically by a few tenths of a percent,<sup>11,13,14</sup> and produces flat and taut membranes.

This built-in pretensioning, together with the large  $E$  values and the low mass density of the monolayers, suggests that it should be possible to self-assemble nanomechanical drumhead resonators of a few micrometers in diameter. Such an approach combines simplicity with versatility, in particular because of the wide range of possibilities for tailoring the properties of nanoparticles and ligands independently. Because of their extremely low mass ( $m \sim 1$  pg), eigenfrequencies ( $f \sim (k/m)^{1/2}$ ) in the megahertz range can be achieved with a low stiffness  $k$ ; a low  $k$  enhances the sensitivity of the nanomechanical dynamics to external forces and increases the resonator's tunability. In this Letter, we demonstrate self-assembled nanomechanical resonators comprised of either gold (Au) or magnetite (Fe<sub>3</sub>O<sub>4</sub>) nanoparticles and compare their

Received: February 17, 2013

Published: April 18, 2013

performance with previously reported ultrathin drumhead resonators, such as those constructed with graphene.<sup>16–21</sup>

Figure 1a,b shows transmission electron microscope (TEM) images of a freestanding monolayer self-assembled from

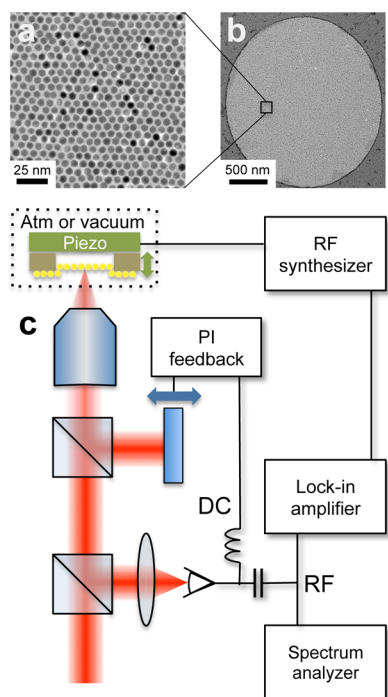


**Figure 1.** Self-assembled Au nanoparticle monolayer drumhead resonators. TEM images of Au nanoparticle monolayer showing (a) individual nanoparticles and (b) complete membrane freely suspended across a 2  $\mu\text{m}$  diameter hole in a 100 nm thick  $\text{Si}_3\text{N}_4$  substrate. (c) Schematic of the laser-interferometric microscope used to detect the high frequency thermal or piezo-driven monolayer vibrations.

$\sim 5.5$  nm diameter Au nanoparticles capped with dodecanethiol ligands. The high-magnification TEM image in Figure 1a reveals the individual nanoparticles that form a close-packed and well-ordered monolayer, which, as is shown in Figure 1b, is strong enough to span a several micrometer-scale prefabricated hole in a silicon-nitride-coated substrate. These self-supporting monolayers are robust and remain intact for months.

To extract the high-frequency nanomechanical dynamics, we developed an interferometric microscopy setup as shown in Figure 1c to measure the out-of-plane motion (displacement  $A$ ) of the resonators. We focus a single-mode laser beam ( $\lambda = 635$  nm) to a diffraction-limited spot (fwhm  $\sim 400$  nm; NA = 0.70) on the sample and interfere the reflected beam with a reference beam in a Michelson geometry as indicated; the interferometer is locked to the edge of a fringe by feeding back to the length of the reference arm and a balanced detector was used to remove common-mode noise. In order to avoid damaging the self-assembled membranes, low optical power ( $<10$   $\mu\text{W}$  in air and  $<500$  nW in vacuum) was typically used in the probe arm and mixed with a much stronger reference beam ( $\sim 100$   $\mu\text{W}$ ) to achieve sub-pm/(Hz)<sup>1/2</sup> sensitivity. Intrinsic thermal excitations were measured with a spectrum analyzer, and vibrations driven by a piezo transducer were probed and imaged by making phase-sensitive measurements with a high-speed lock-in amplifier. The sample could be translated laterally for imaging and was mounted in an enclosure that could be evacuated for measurements in vacuum.

To investigate the effect of drumhead size, we first present data for Au monolayer resonators of different diameters  $d$ . A typical measurement of the power spectral density  $S(f)$  of a thermally excited (300 K) self-assembled resonator ( $d \sim 9$   $\mu\text{m}$ ) under ambient conditions is shown in Figure 2a. The two

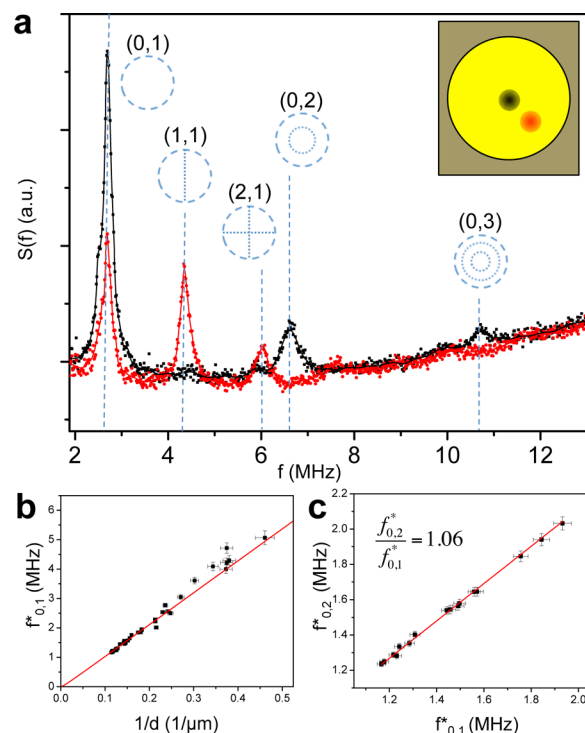


**Figure 2.** Power spectral density of thermal motion. (a) Power spectral density (a.u.) of a  $\sim 9$   $\mu\text{m}$  diameter Au monolayer in air, thermally excited by thermal fluctuations at room temperature. The two traces show spectra measured at the center of the monolayer (black) and halfway between the center and the perimeter (red), as indicated in the inset. The peaks are identified with a predicted mode and sketches of the nodal pattern are shown. (b) Dependence of the effective frequencies,  $f^* = f/K$  (see eq 1 and text), on drumhead diameter  $d$  for 35 Au monolayer devices of different diameter (2–10  $\mu\text{m}$ ) and eccentricity (0.27–0.5);  $d$  is taken to be the membrane width along the minor axis. The solid line is the prediction of eq 1, including the  $d$ -dependent added mass due to air loading. (c) Effective resonant frequency  $f^*$  of the (0,2) mode versus the effective frequency  $f^*$  of the (0,1) mode for 16 drumheads (a subset of the devices shown in panel b). The ratio is slightly larger than 1, suggesting stronger inertial loading for the (0,1) mode. In panels b and c, the error bars reflect the experimental uncertainties in the frequency measurements and in the determination of drumhead size and ellipticity.

spectra are recorded with the laser spot positioned in the center (black) and off-center (red) of the membrane, allowing us to observe both azimuthally isotropic and anisotropic modes.

For circular drumheads, the normal modes are indexed by two quantities; the first index  $m$  denotes the number of radial nodal lines and the second index  $n$  the number of azimuthal nodal lines (including along the circumference). Linear elastic theory for clamped membranes under tension  $\tau$ , of areal mass density  $\sigma$ , and with negligible bending stiffness, leads to the following expression for the natural resonant frequencies in vacuum<sup>22,23</sup>

$$f_{m,n} = \frac{K_{m,n}}{\pi d} \sqrt{\frac{\tau}{\sigma}} \quad (1)$$

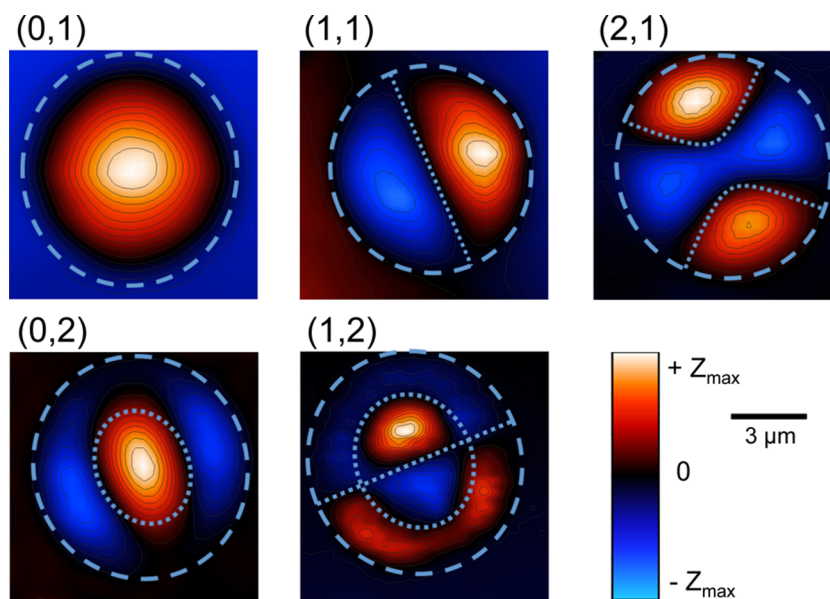


**Figure 3.** Laser-interferometric images of drumhead normal modes. Images were taken on  $\sim 9 \mu\text{m}$  diameter Au monolayer resonators at room temperature under vacuum ( $2.5 \times 10^{-6}$  mbar), driven by a piezo transducer (three different samples; (0,2), (2,1), and (1,2) are from the same sample). Red and blue indicate displacement into and out of the plane, respectively, and nodal lines appear dark. The maximum amplitude in these images is on the order of 1 nm. Dashed lines show the actual drumhead perimeters; dotted lines give the nodal patterns predicted by membrane theory.

where the constant  $K_{m,n}$  depends on the mode indices  $(m, n)$ . In the case of a circular drumhead,  $K_{m,n}$  is the  $n$ -th positive root of the  $m$ -th order Bessel function. For resonators with an ellipticity  $e$ , the node pattern is more complex and the coefficient  $K_{m,n}$  is determined numerically.<sup>22,23</sup>

Comparing eq 1 to the spectra in Figure 2a, we can assign the observed resonance peaks to normal resonator modes that are consistent with the expected frequency and mode shape, as indicated in the figure. For example, the spectrum taken in the center of the membrane (black) is only sensitive to  $m = 0$  modes, whereas the  $m \neq 0$  modes are only observed when the laser beam is positioned off-center (red).

In order to explore the size dependence predicted in eq 1 for our devices, we plot the resonance peak frequencies  $f_{m,n}^*$  for 35 different monolayer drumheads as a function of their inverse diameter  $1/d$  in Figure 2b; we divided out the mode and eccentricity dependence by defining an effective frequency  $f_{m,n}^* \equiv f_{m,n}/K_{m,n}$  and took the diameter  $d$  to be the width along the minor axis. Over the frequency range examined,  $f^*$  generally follows the simple  $1/d$  dependence of eq 1. Improved agreement can be achieved by taking into account air loading of the membrane, which plays a significant role for the larger membranes and increases their effective mass. To account for this quantitatively, we replace  $\sigma$  by  $[\sigma + (4/3\pi)d\rho_0]$ , where  $\rho_0$  is the density of air.<sup>24</sup> Here, the second term is a correction for macroscopic drumheads to estimate the additional inertial mass due to the acceleration of the surrounding air by the vibrating drumheads. Using this correction together with  $\sigma = 4.2 \times 10^{-5}$  kg/m<sup>2</sup> calculated from the nanoparticles' size and packing arrangement (obtained from TEM) and from estimates of the ligand density, the measured  $f^*$  are well parametrized by eq 1 as seen by the solid red line in Figure 2b.

Air loading is expected to affect each mode differently. An increase in mode number produces a flow field with a smaller characteristic length scale and higher frequency. This reduces the inertial load experienced by the device<sup>25</sup> with the resonant

frequencies approaching the frequencies in vacuum for infinite mode number. In Figure 2c, we plot the measured effective frequency  $f^*$  of the (0,2) mode versus the effective frequency  $f^*$  of the (0,1) mode for the same 35 devices. The observed value 1.06 for the mode ratio  $f_{0,2}^*/f_{0,1}^*$  confirms that the (0,1) mode frequency is lowered more than the (0,2) mode frequency by a few percent (Figure 2c).

Two aspects emerging from the data in Figure 2 are noteworthy. First, as eq 1 captures the behavior of the nanoparticle membrane resonators very well, we can conclude that the nanoparticle monolayers operate in the limit of negligible bending stiffness (adding terms to account for bending<sup>24</sup> shifts the resonant frequencies by 0.4% at most). Second, the data in Figure 2b reveal only a small amount of scatter, indicating that the resulting line tension  $\tau$  is quite constant for different membranes prepared in the same process: using eq 1 and the areal mass  $\sigma$  determined from TEM we determine the tension in the membranes to be  $\tau = (0.048 \pm 0.005)$  N/m.

This nearly constant tension value stands in contrast to the widespread (>100%) in Young's moduli observed previously in freestanding Au monolayers.<sup>11,13</sup> We believe this is a consequence of the draping process itself; as a nanoparticle layer dries onto the substrate, it bends over the edge of the hole and attaches to the hole's walls, receding into the hole and thereby tightening the freestanding portion until its line tension  $\tau$  becomes equal to the maximum attachment strength. This strength is set by van der Waals interactions between the nanoparticle sheet and the substrate; therefore, the line tension  $\tau$  can be equated with the adhesion energy per unit area between silicon nitride and the monolayers. It is likely to be similar for similar drying procedures and substrates, regardless of a particular monolayer's elastic properties. Since the tension is the product of Young's modulus and prestrain, its constancy implies that the draping process automatically adjusts such that slightly stiffer (softer) membranes will experience less (more)

prestrain. As the frequency depends directly on  $\tau$ , this implies good control despite the simplicity of the drying-mediated fabrication process.

By translating the sample under the focused laser spot with an  $x$ - $y$  translation stage, we were able to image the normal modes directly. In order to perform phase-sensitive detection of the membrane motion, we drove the sample with a piezo transducer in a vacuum and used a lock-in amplifier to extract the interferometric signal due to the resonating membrane. Figure 3 shows the spatial amplitude patterns with red and blue indicating displacement into and out of the plane, respectively. Their nodal lines are in excellent agreement with membrane theory<sup>22,23</sup> as shown by the dotted lines that are plotted to scale using the monolayers' actual sizes and eccentricity. Because of the slight eccentricity of the membrane, the imaged (2,1) and (0,2) modes (which are closely spaced in frequency) are a mixture of the (2,1) and (0,2) modes of a perfect circle. The vibration patterns are not affected by the discreteness of the nanoparticles or by imperfections in their arrangement (including grain boundaries), as these features are much smaller than the wavelengths of the modes at these membrane sizes.

Dissipation of the mechanical excitation from factors like clamping and intrinsic material properties can be characterized by the quality factor  $Q$ , which is proportional to the ratio of maximum energy stored in the device to the energy dissipated per cycle. While  $Q$  was limited to  $\sim 10$  in air (Figure 2), measurements of the resonators in vacuum showed that the  $Q$  improved more than 1 order of magnitude when air damping (due to a combination of viscous and acoustic effects) was absent. In Figure 4, we show  $|A(f)|^2$  for (0,1) resonance

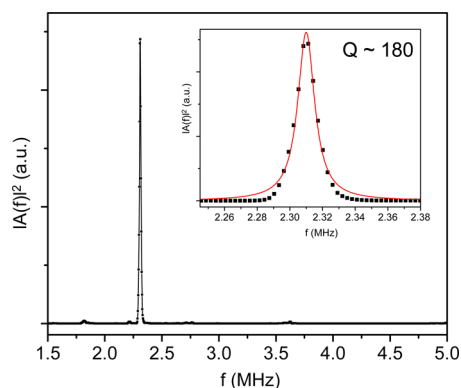


**Figure 4.** Quality Factor. Resonance peak for the fundamental mode of  $d \sim 6 \mu\text{m}$  diameter Au monolayer drumhead at room temperature, excited under vacuum ( $2.5 \times 10^{-6}$  mbar) by a piezo transducer. Inset: zoomed-in view around  $f = 2.3$  MHz. A Lorentzian fit to the line is shown and reveals  $Q \sim 180$  (see Supporting Information).

obtained by driving a  $d \sim 6 \mu\text{m}$  resonator piezoelectrically in vacuum; a Lorentzian fit shown in the inset reveals  $Q \sim 180$ . This value is comparable to room temperature results on graphene drumhead resonators of similar size, fabricated by CVD ( $Q \sim 700$ ) or mechanical exfoliation ( $Q \sim 25$ – $300$ ).<sup>18–20,26</sup> In general,  $Q$  is expected to increase with membrane size, and data on graphene drumheads suggests<sup>16</sup> that  $Q$  is quite sensitive to changes in diameter below sizes of about  $10 \mu\text{m}$ , which corresponds to the size range of the systems reported here. For example, we measured  $Q \sim 500$  for a larger,  $d \sim 9 \mu\text{m}$  monolayer in vacuum (see Supporting

Information, Figure S2). It may be possible to improve  $Q$  by moving toward larger freestanding sheets or possibly going to higher-order modes.<sup>27</sup> Nevertheless, for a drumhead material whose structural integrity depends on short hydrocarbon chains, these results are already remarkable. Our  $Q$  values exceed those for mechanical resonators based on poly(methyl methacrylate) (PMMA)<sup>28</sup> and are an order of magnitude higher than for polydimethylsiloxane (PDMS) resonators.<sup>29</sup> Comparison of their damping based on these measured  $Q$  values would require characterization of the relative importance of tension and bending in the membranes in addition to their clamping conditions.

A special feature of the resonators introduced here is that the same self-assembly method can be employed to form drumheads of different geometry or thickness (using multilayer films), from nanoparticles with different composition, size, and ligand groups on a variety of substrates. Importantly, as the wavelengths of the vibration modes in this study are 2 orders of magnitude greater than the nanoparticle sizes, the local ordering and the granularity of the nanoparticle sheets as a result of particle polydispersity as well as domain formation during self-assembly are not crucial. As long as they form intact layers that are sufficiently uniform in average thickness, our analysis based on material properties for linear elasticity theory is applicable. Figure 5 gives an indication of this versatility,

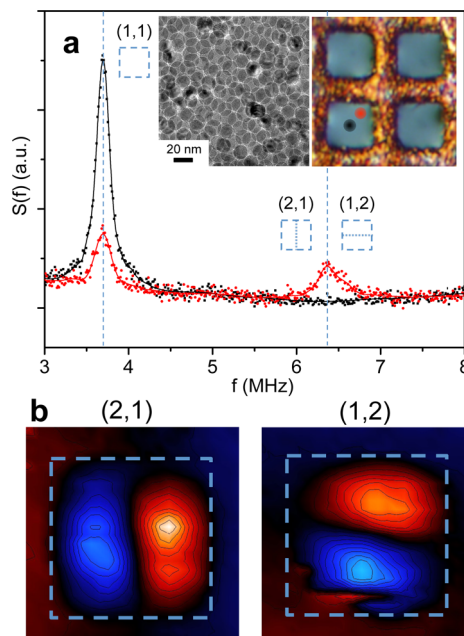


**Figure 5.**  $\text{Fe}_3\text{O}_4$  drumheads. Square drumheads self-assembled from  $\text{Fe}_3\text{O}_4$  particles onto empty commercial TEM grids (SPI Supplies 2155C-XA). The holes have  $7.5 \mu\text{m}$  side length. (a) Power spectrum for a multilayer drumhead in air excited by thermal fluctuations at room temperature. Inset: TEM detail (top-left) and optical micrograph of the TEM grid (top-right). The traces show the power spectrum measured at the center of the drumhead (black) and off-center (red). Modes (1,2) and (2,1) have nearly identical resonance frequencies. Sketches of the nodal pattern for these modes are shown above the peaks. Note that local disorder does not affect the spectrum as long as the layers are uniform over distances of the order of the wavelength. (b) Laser-interferometric images of the nearly degenerate (1,2) and (2,1) modes in (a), taken in vacuum and with piezo actuation of the membrane. The maximum amplitude in these images is  $\sim 1$  nm.

showing freestanding disordered Fe<sub>3</sub>O<sub>4</sub> nanoparticle multilayer (Figure 5a) drumheads, self-assembled by drying oleic-acid-ligated Fe<sub>3</sub>O<sub>4</sub> nanoparticles over a bare copper TEM grid with square holes of side length  $L = 7.5 \mu\text{m}$  (ordered Fe<sub>3</sub>O<sub>4</sub> nanoparticle monolayer drumheads are shown in Supporting Information, Figure S3). The same general form, eq 1, for the resonance frequencies is still valid, except that for a square membrane the diameter  $d$  is replaced by  $L$  and  $K$ , which reflects the square geometry. Specifically, modes  $(m, n)$  exhibit degeneracy according to  $K_{m,n} \propto (m^2 + n^2)^{1/2}$ . While difficult to resolve under thermal excitation, the slight difference in lengths between the sides results in two modes clearly imaged in Figures 5b for the (2,1) and (1,2) eigenmodes under piezo excitation.

Our results demonstrate a new class of robust drumhead nanoresonators self-assembled through simple wet chemistry methods from functionalizable nanoparticle building blocks. The versatile array of available nanoparticles provides a means for coupling plasmonic, magnetic, optical, and electronic interactions to nanomechanical motion. The extremely low mass and low stiffness of these resonators promises an enhanced mechanical sensitivity to external forces, providing both a potential path to sensing applications<sup>19</sup> and to the control of nanomechanical motion.<sup>21</sup> Furthermore, the simple self-assembly process could be exploited to develop more complex nanomechanical systems with expanded functionality. Membranes could be modified after self-assembly by using focused ion or electron beams for shaping or tensioning.<sup>14</sup> Additionally, by draping monolayers over a large number of nearby, arbitrarily shaped holes, it may be possible to develop coupled resonator systems that could serve as mechanical band-pass filters.<sup>30</sup>

## ■ ASSOCIATED CONTENT

### Supporting Information

Additional information and figures. This material is available free of charge via the Internet at <http://pubs.acs.org>.

## ■ AUTHOR INFORMATION

### Corresponding Author

\*E-mail: [jrguest@anl.gov](mailto:jrguest@anl.gov).

### Notes

The authors declare no competing financial interest.

## ■ ACKNOWLEDGMENTS

We thank Tom Witten, Edward Barry, Yifan Wang, Daniel Lopez, and Dmitri Talapin for helpful discussions and Ralu Divan, Justin Jureller, and Qiti Guo for chip fabrication techniques and technical assistance. This work was supported by NSF through DMR-1207204. The Chicago MRSEC, supported by NSF DMR-0820054, is gratefully acknowledged for access to its shared experimental facilities. J.E.S. acknowledges support from the Australian Research Council grants scheme. Use of the Center for Nanoscale Materials was supported by the U.S. Department of Energy, Office of Science, Office of Basic Energy Sciences, under Contract No. DE-AC02-06CH11357.

## ■ REFERENCES

- (1) Shipway, A. N.; Katz, E.; Willner, I. *ChemPhysChem* **2000**, *1*, 18.
- (2) Gur, I.; Fromer, N. A.; Geier, M. L.; Alivisatos, A. P. *Science* **2005**, *310*, 462.
- (3) Saunders, A. E.; Shah, P. S.; Sigman, M. B.; Hanrath, T.; Hwang, H. S.; Lim, K. T.; Johnston, K. P.; Korgel, B. A. *Nano Lett.* **2004**, *4*, 1943.
- (4) Shevchenko, E. V.; Talapin, D. V.; Kotov, N. A.; O'Brien, S.; Murray, C. B. *Nature* **2006**, *439*, 55.
- (5) Murray, C.; Kagan, C.; Bawendi, M. *Annu. Rev. Mater. Sci.* **2000**, *30*, 545.
- (6) Park, J.; An, K.; Hwang, Y.; Park, J.-G.; Noh, H.-J.; Kim, J.-Y.; Park, J.-H.; Hwang, N.-M.; Hyeon, T. *Nat. Mater.* **2004**, *3*, 891.
- (7) Lin, X. M.; Jaeger, H. M.; Sorensen, C. M.; Klabunde, K. J. *J. Phys. Chem. B* **2001**, *105*, 3353.
- (8) Dong, A.; Chen, J.; Vora, P. M.; Kikkawa, J. M.; Murray, C. B. *Nature* **2010**, *466*, 474.
- (9) Dong, A.; Ye, X.; Chen, J.; Murray, C. B. *Nano Lett.* **2011**, *11*, 1804.
- (10) Eah, S.-K. *J. Mater. Chem.* **2011**, *21*, 16866.
- (11) Mueggenburg, K. E.; Lin, X.-M.; Goldsmith, R. H.; Jaeger, H. M. *Nat. Mater.* **2007**, *6*, 656.
- (12) Cheng, W.; Campolongo, M. J.; Cha, J. J.; Tan, S. J.; Umbach, C. C.; Muller, D. A.; Luo, D. *Nat. Mater.* **2009**, *8*, 519.
- (13) He, J.; Kanjanaboos, P.; Frazer, N. L.; Weis, A.; Lin, X.-M.; Jaeger, H. M. *Small* **2010**, *6*, 1449.
- (14) Kanjanaboos, P.; Joshi-Imre, A.; Lin, X.-M.; Jaeger, H. M. *Nano Lett.* **2011**, *11*, 2567.
- (15) He, J.; Lin, X.-M.; Chan, H.; Vuković, L.; Král, P.; Jaeger, H. M. *Nano Lett.* **2011**, *11*, 2430.
- (16) Barton, R. A.; Parpia, J.; Craighead, H. G. *J. Vac. Sci. Technol., B* **2011**, *29*, 050801.
- (17) Garcia-Sanchez, D.; van der Zande, A. M.; Paulo, A. S.; Lassagne, B.; McEuen, P. L.; Bachtold, A. *Nano Lett.* **2008**, *8*, 1399.
- (18) Barton, R. A.; Ilic, B.; van der Zande, A. M.; Whitney, W. S.; McEuen, P. L.; Parpia, J. M.; Craighead, H. G. *Nano Lett.* **2011**, *11*, 1232.
- (19) Bunch, J. S.; van der Zande, A. M.; Verbridge, S. S.; Frank, I. W.; Tanenbaum, D. M.; Parpia, J. M.; Craighead, H. G.; McEuen, P. L. *Science* **2007**, *315*, 490.
- (20) Singh, V.; Sengupta, S.; Solanki, H. S.; Dhall, R.; Allain, A.; Dhara, S.; Pant, P.; Deshmukh, M. M. *Nanotechnology* **2010**, *21*, 165204.
- (21) Barton, R. A.; Storch, I. R.; Adiga, V. P.; Sakakibara, R.; Cipriani, B. R.; Ilic, B.; Wang, S. P.; Ong, P.; McEuen, P. L.; Parpia, J. M.; Craighead, H. G. *Nano Lett.* **2012**, *12*, 4681.
- (22) Troesch, B.; Troesch, H. *Math Comput.* **1973**, *27*, 755.
- (23) Neves, A. G. M. *Commun. Pure Appl. Anal.* **2010**, *9*, 611.
- (24) Fletcher, N. H.; Rossing, T. D. *The Physics of Musical Instruments*; Springer Verlag, 1998.
- (25) Van Eysden, C. A.; Sader, J. E. *J. Appl. Phys.* **2007**, *101*, 044908.
- (26) Bunch, J.; Verbridge, S.; Alden, J.; van der Zande, A.; Parpia, J.; Craighead, H.; McEuen, P. *Nano Lett.* **2008**, *8*, 2458.
- (27) Adiga, V.; Ilic, B.; Barton, R.; Wilson-Rae, I.; Craighead, H.; Parpia, J. *Appl. Phys. Lett.* **2011**, *99*, 253103.
- (28) Zhang, G.; Gaspar, J.; Chu, V.; Conde, J. *Appl. Phys. Lett.* **2005**, *87*, 104104.
- (29) Dubois, P.; Rosset, S.; Niklaus, M.; Dadras, M.; Shea, H. J. *Microelectromech. Syst.* **2008**, *17*, 1072.
- (30) Greywall, D. S.; Busch, P. A. *J. Micromech. Microeng.* **2002**, *12*, 925.